Identification of the critical depth-of-cut through 2-D image of the cutting region resulted from taper cutting of brittle materials

Wen Gu[a], Zhiwei Zhu[a,b,†], Wu-Le Zhu[c], Leyao Lu[a], Suet To[b], and Gaobo Xiao[b]

a. School of Mechanical Engineering, Nanjing University of Science and Technology, Nanjing, J.S. 210094, China

b. State Key Laboratory of Ultra-precision Machining Technology, Department of Industrial and Systems Engineering, The Hong Kong Polytechnic University, Kowloon, Hong Kong SAR, China

c. Department of Micro-Engineering, Kyoto University, Nishikyo-ku, Kyoto, 615-8540, Japan

†. Corresponding author: zw.zhu@njust.edu.cn

Abstract

An automatic identification method for obtaining the critical depth-of-cut (DoC) of brittle materials with nanometric accuracy and sub-nanometric uncertainty is proposed in this paper. With this method, two-dimensional (2-D) microscopic image of the taper cutting region is captured and further processed by image analysis to extract the margin of generated micro-cracks in the imaging plane. Meanwhile, the analytical model is formulated to describe the theoretical curve of the projected cutting points on the imaging plane with respect to a specified DoC during the whole cutting process. By adopting the differential evolution algorithm based minimization, the critical DoC can be identified by minimizing the deviation between the extracted margin and the theoretical curve. The proposed method is demonstrated through both numerical simulation and experimental analysis. Compared with conventional 2-D and 3-D microscopic image based methods, determination of the critical DoC in this study uses the envelope profile rather than the onset point of the generated cracks, providing a more objective approach with smaller uncertainty.

Keywords: Diamond cutting; brittle material; critical depth-of-cut; differential evolution algorithm

1. Introduction

Optical materials play a key role in both imaging and non-imaging optical systems. However, a large volume of the materials suffers from low fracture toughness and appears to be brittle in nature, including the optical crystals, infrared optical glasses, transparent ceramics to mention a few [1–3]. For practical applications, ultra-precision diamond turning and diamond milling are commonly adopted to directly generate optical surfaces with complicated shapes on the optical materials. For instance, the freeform Alvarez lens in the mid-wave infrared was generated on single crystal germanium through ductile milling [4], and the discontinuous Fresnel structure was successfully obtained on germanium by means of diamond turning [5]. Moreover, taking advantage of the tool servo assisted diamond turning, more complicated freeform surfaces [6], microstructured lens array [7, 8], and hierarchical microstructures [9] were also generated on optical brittle materials.

To facilitate the diamond cutting process, efforts have been devoted to studies on the underlying mechanism for material removal, mainly focusing on the brittle-ductile transition behavior [2, 7, 10, 11]. The critical depth-of-cut (DoC), at which the brittle-ductile transition occurs, directly reflects the machinability of the material under the specified cutting conditions, attracting intensive investigations from both theoretical [12] and experimental aspects [1, 2, 11]. No matter which aspect is focused, experimental determination of the critical DoC is commonly employed based on the taper cutting featuring linearly varying DoC. After cutting, microscopic image of the cutting region is accordingly taken for the determination of the DoC. In general, there are two sorts of imaging methods for surface characterization, namely the optical microscopy based two-dimensional (2-D) imaging method and the more predominant optical surface profiler based 3-D imaging method [1, 13].

Although the 3-D imaging method provides more detailed information of surface topography in the cutting region [1, 12, 14, 15], micro-cracks in the 2-D image is more obvious to be identified due

to the high contrast between the cracked and optical surfaces, and also, the facility required for the 2-D image is much cheaper and more widespread to access [13, 16]. With the 2-D imaging method, the process starts with the measurement of the groove width at the onset point of the micro-cracks in the image and accordingly calculates the critical DoC from the simple geometry relationship of the employed tool [13]. However, measurement of the groove width in the image is really subjective with large uncertainty, and the influence of the spatial angular discrepancy between the imaging plane and the workpiece surface on the measured width of the groove is ignored. In addition, determination of the onset point of the micro-cracks for both 2-D and 3-D imaging methods is also very subjective without consistency, inevitably leading to low estimation accuracy with poor convergence for the critical DoC. Moreover, the manual handling in both the 2-D and 3-D imaging methods is laborious and time-consuming, especially for processing a large volume of captured images.

To overcome the aforementioned defects in determining the critical DoC, an automatic identification method is proposed based on the 2-D image analysis. For determining the critical DoC, searching for the onset point of the micro-cracks in conventional methods is replaced by extracting envelope curve of the whole cracking region, which may significantly improve the estimation uncertainty. Furthermore, by best-fitting the envelope curve of the micro-cracks with the projected theoretical profile of the cutting points with a specified DoC, the critical DoC can be effectively identified.

2. Characteristics of the cutting region

To identify the critical DoC for brittle materials, schematic of the commonly adopted taper cutting is illustrated in Fig. 1 (a). During cutting, the diamond tool moves straightly with a constant velocity v_{t}. Meanwhile, the sample is fixed with an inclination angle γ related to the

moving direction of the diamond tool, leading to the cutting with linearly varying DoC. Thereby, a cutting region with both smooth and crack features is obtained, respectively suffering from ductile and brittle mode material removal with practical DoC being smaller and larger than the critical DoC.

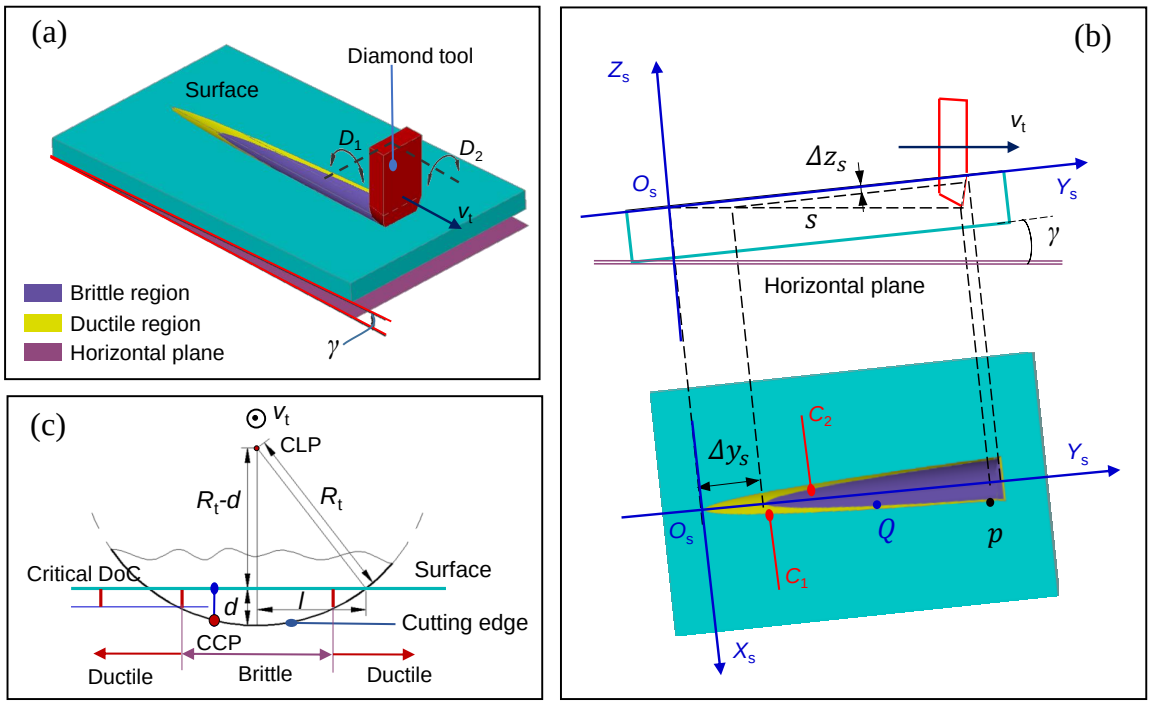

Figure 1: Schematic of the cutting system, (a) 3-D view of the taper cutting, (b) the side and top views of the cutting system, and (c) geometric relatinship for practical DoC.

As shown in Fig. 1 (a), taking the horizontal plane as the reference, there are two inevitable installation angles of the cutting tool around the D_1 and D_2 directions. Since the tool edge is round, influences of rotation around the D_2 direction on features of the cutting region can be ignored. On the other hand, the rotation around the D_1 direction can be regarded as a part of the inclination angle γ.

To give a mathematical description of the cutting region, a fixed Cartesian coordinate system $O_s - X_sY_sZ_s$ is firstly defined, where the $O_s - X_sY_s$ plane and the to-be-machined surface of the sample without inclination are coplanar and set as the observation plane for modeling. The origin

point O_s is coincident with the initial cutting point, and the O_sY_s axis and the direction vector of the cutting velocity are in the same plane. From the projection relationship shown in Fig. 1 (c), it shows that the practical DoC may vary with respect to the cutter contact point (CCP) at the round tool edge, resulting in both ductile and brittle mode removals of the material for any one cutter location point (CLP). After cutting, there are two characteristic curves in the cutting region, namely the curve C_1 and C_2 as shown in Fig. 1 (b). The curve C_1 is the intersection between the moving tool and the sample surface, and the curve C_2 is the envelope of the cracked region. In general, the practical DoC for an arbitrary point in the envelope may be equal to the critical DoC.

For the point $p(x_\mathrm{p}, y_\mathrm{p}, 0)$ at the curve C_1, the coordinate values can be derived from the geometric relationship shown in Fig. 1 (c) as $x_\mathrm{p} = \sqrt{R_\mathrm{t}^2 - (R_\mathrm{t} - d)^2}$, and $y_\mathrm{p} = s(\cos\gamma)^{-1}$, where s is the moving distance of the tool, R_t is the nose radius of the diamond tool, and d is the distance from the tool tip to the free surface, and Δy_s and Δz_s are.. Therefore, taking s as the parametric variable, profile of the curve C_1 can be expressed by

$$\begin{cases} x_1 = \pm\sqrt{R_\mathrm{t}^2 - (R_\mathrm{t} - s\tan\gamma)^2} \\ y_1 = s(\cos\gamma)^{-1} \\ z_1 = 0 \end{cases} \tag{1}$$

With the envelope curve C_2, it has the same shape with the curve C_1, and can be derived by translating curve C_1 along the O_sY_s and O_sZ_s directions with distances of $\Delta y_\mathrm{s} = h_\mathrm{c}(\tan\gamma)^{-1}$ and $\Delta z_\mathrm{s} = -h_\mathrm{c}$ as

$$\begin{cases} x_2 = \pm\sqrt{R_\mathrm{t}^2 - (R_\mathrm{t} - s\tan\gamma)^2} \\ y_2 = s(\cos\gamma)^{-1} + h_\mathrm{c}(\tan\gamma)^{-1} \\ z_1 = -h_\mathrm{c} \end{cases} \tag{2}$$

where h_c denotes the critical DoC.

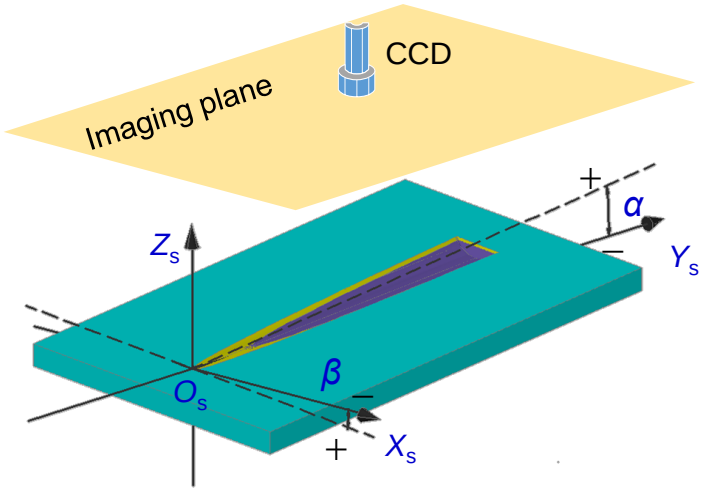

Figure 2: Schematic of the microscopy system for cutting region imaging.

When capturing the cutting region through optical microscopy, the observation plane $O_s - X_sY_s$ is parallel with the imaging plane of the microscopy. As for the installation of the sample in the microscopy system, there will be inevitable angular discrepancy around both the O_sX_s and O_sY_s axes as illustrated in Fig. 2. Considering an arbitrary point $Q(x_2, y_2, z_2)$ at the curve C_2 in the $O_s - X_sY_sZ_s$ system, after rotating around the O_sX_s axis with an angle of α, the new position of the point Q in the $O_s - X_sY_sZ_s$ system can be expressed by

$$\begin{cases} x_{\mathrm{r1}} = x_2 \\ y_{\mathrm{r1}} = \sqrt{y_2^2 + z_2^2}\cos\theta_1 \\ z_{\mathrm{r1}} = -\sqrt{y_2^2 + z_2^2}\sin\theta_1 \end{cases} \tag{3}$$

with

$$\theta_1 = \arctan\left(-\frac{z_2}{y_2}\right) - \alpha \tag{4}$$

Similarly, after rotating around the symmetric axis of the curve C_1 with an angle of β, the point

Q will reach a new position as expressed by

$$\begin{cases} x_{\mathrm{r}2} = -\sqrt{x_2^2 + z_2^2}\sin\theta_2 \\ y_{\mathrm{r}2} = y_{r1} + \left(\sqrt{x_2^2 + z_2^2}\cos\theta_2 - |z_2|\right)\sin\alpha \\ z_{\mathrm{r}2} = z_{r1} - \left(\sqrt{x_2^2 + z_2^2}\cos\theta_2 - |z_2|\right)\cos\alpha \end{cases} \tag{5}$$

with

$$\theta_2 = \arctan\left(\frac{x_2}{z_2}\right) + \beta \tag{6}$$

Therefore, the projection profile of the envelope curve C_2 in the imaging plane, namely the envelope of the cracked region in the image taken, can be obtained as

$$\begin{cases} x_{\mathrm{e}} = -\sqrt{x_2^2 + z_2^2}\sin\theta_2 \\ y_{\mathrm{e}} = \sqrt{y_2^2 + z_2^2}\cos\theta_1 + \left(\sqrt{x_2^2 + z_2^2}\cos\theta_2 - |z_2|\right)\sin\alpha \end{cases} \tag{7}$$

3. Identification principle

3.1. Problem Statement

As discussed in Section 2, there are four parameters governing the envelope curve C_2, namely $P_1 = [\alpha, \beta, \gamma, h_{\mathrm{c}}]$. Practically, the margin of the cracked region can be automatically extracted through image analysis of the microscopic image taken. By comparing the theoretical curve and the practical margin, it will be very promising to get an accurate estimation of the critical DoC. In general, there are two key problems to be addressed before conducting the comparison between the theoretical and practical curves: a) the coordinate system mismatching; and b) one-one correspondence for points in the theoretical and practical curves.

- As for the coordinate system mismatching, the theoretical curve in Eq. (7) is described in the $O_s - X_sY_sZ_s$ system. Whereas, the extracted margin of the cracked region is described

in its local coordinate system. With an arbitrary point $P_{\mathrm{m}}(x_{\mathrm{m}}, y_{\mathrm{m}})$ at the margin, its new coordinates after planar position transition can be expressed by

$$\begin{bmatrix} \hat{x}_{\mathrm{m}} \\ \hat{y}_{\mathrm{m}} \end{bmatrix} = \begin{bmatrix} \cos\kappa & -\sin\kappa \\ \sin\kappa & \cos\kappa \end{bmatrix} \begin{bmatrix} x_{\mathrm{m}} \\ y_{\mathrm{m}} \end{bmatrix} - \begin{bmatrix} x_{\mathrm{o}} \\ y_{\mathrm{o}} \end{bmatrix} \tag{8}$$

where $[x_{\mathrm{o}}, y_{\mathrm{o}}]^{\mathrm{T}}$ and κ are the planar position translation vector and the rotational angle around the O_sZ_s axis, respectively. The position transition as presented in Eq. (8) is to align the local coordinate system of the captured image to be consistent with the pre-defined $O_s - X_sY_sZ_s$ system.

- The description of the theoretical curve is based on a parametric equation as given in Eq. 2 and Eq. 7, which is difficult to derive an explicit expression to directly relate the two variables x_{e} and y_{e}. By adopting $S(\cdot)$ to denote the cubic spline interpolation function, the curve can then be directly described through the two variables as $x_{\mathrm{e}} = S(y_{\mathrm{e}})$. With respect to the point at the margin $[\hat{x}_{\mathrm{m}}, \hat{y}_{\mathrm{m}}]$, coordinates of the corresponding point at the theoretical curve C_2 yield $[S(\hat{y}_{\mathrm{m}}), \hat{y}_{\mathrm{m}}]^{\mathrm{T}}$. Thereby, the distance between the two points at the margin and the theoretical curve can be accordingly determined by $d = |S(\hat{y}_{\mathrm{m}}) - \hat{x}_{\mathrm{m}}|$.

Therefore, the identification of the critical DoC lies in the determination of a set of proper parameters to minimize the deviation between positions of points at the margin of the cracked region and the corresponding points at the theoretical curve C_2. Mathematically, it takes the form of

$$\min E = \sqrt{\frac{\sum_{n=1}^{N} d_n^2}{N}} = \sqrt{\frac{\sum_{n=1}^{N} \left[S(\hat{y}_{\mathrm{m}}^{(n)}) - \hat{x}_{\mathrm{m}}^{(n)} \right]^2}{N}} \tag{9}$$

where N denotes the number of the points extracted from the margin of the cracked region.

From the objective function shown in Eq. (9), except for the four governing the curve C_2, there are another three unknown parameters $P_2 = [x_{\mathrm{o}}, y_{\mathrm{o}}, \kappa]$ for the planar position transition to

be identified. Obviously, it is a multi-dimensional minimization problem with strong nonlinearity. The differential evolution (DE) algorithm which is a simple but very powerful tool to solve global optimization problems is employed in this study to minimize the objective function to identify the critical DoC h_{c}.

3.2. Differential evolution based minimization

The DE algorithm which belongs to the evolutionary computation uses differential computation as the basic operation. It mainly consists of four phases, namely the initialization, mutation, crossover, and selection [17]. With the problem as discussed above, there are seven parameters to be determined to minimize the objective function as shown in Eq. (9). The parameters can be expressed in the vector form as $\mathbf{P} = [\alpha, \beta, \gamma, h_{\mathrm{c}}, x_{\mathrm{o}}, y_{\mathrm{o}}, \kappa]$.

At the initialization phase, the initial population is constructed through uniform randomization within the searching space. Mathematically, the population is obtained as [18]

$$\mathbf{P}_{\mathrm{o}}^{(K,L)} = \mathbf{P}_{\min}^{(K,L)} + \left(\mathbf{P}_{\max}^{(K,L)} - \mathbf{P}_{\min}^{(K,L)}\right) \cdot \mathbf{\Omega}^{(L,L)} \tag{10}$$

where K and L are the population size and the numbers of parameters (i.e. $L = 7$), $\mathbf{P}_{\min}^{(K,L)}$ and $\mathbf{P}_{\max}^{(K,L)}$ are the lower and upper boundaries of the searching space, and each boundary is a K by L matrix. $\mathbf{\Omega}^{(L,L)}$ is the uniformly distributed random matrix with size of L by L, and each of the random number in the matrix ranges from 0 to 1.

After the initialization, a mutation operation based on differential computation is adopted to generate a mutant population, leading to the target vector $\hat{\mathbf{P}}_{\mathrm{o}}^{(k,L)}$ (the k-th column in the mutant population $\hat{\mathbf{P}}_{\mathrm{o}}^{(K,L)}$) as [17]

$$\hat{\mathbf{P}}_{\mathrm{o}}^{(k,L)} = \mathbf{P}_{\mathrm{o}}^{(k_1,L)} + F_k \cdot \left(\mathbf{P}_{\mathrm{o}}^{(k_2,L)} - \mathbf{P}_{\mathrm{o}}^{(k_3,L)}\right) \tag{11}$$

where $k_i,\ i = 1, 2, 3$ are mutually exclusive integers ranging from 1 to K, and $F_k \in [0, 2]$ is the mutation factor for scaling the difference vector.

To increase the diversity of the population, the crossover operation is further introduced to form a trial vector $\mathbf{P}_{\text{tr}}^{(k,l)}$, where the number in the k-th column and l-th row can be expressed by [17, 18]

$$P_{\text{tr}}^{(k,l)} = \begin{cases} \hat{P}_{\text{o}}^{(k,l)},\ if\ \Psi_k \leq CR\ or\ k = \zeta_l \\ P_{\text{o}}^{(k,l)},\ otherwise \end{cases} \tag{12}$$

where $\Psi_k \in [0, 1]$ is a uniform random number, and $CR \in [0, 1]$ is the crossover factor. ζ_l is a random integer ranging from 1 to K.

After the crossover operation, the selection process following the greedy criterion is conducted between the two populations $\mathbf{P}_{\text{tr}}^{(K,L)}$ and $\mathbf{P}_{\text{o}}^{(K,L)}$ to form the next generation population $\mathbf{P}_{\text{new}}^{(K,L)}$ [17]. For the vector in the k-th column, the selection process can be described by

$$\mathbf{P}_{\text{new}}^{(k,L)} = \begin{cases} \mathbf{P}_{\text{o}}^{(k,L)},\ if\ E\left(\mathbf{P}_{\text{o}}^{(k,L)}\right) \leq E\left(\mathbf{P}_{\text{tr}}^{(k,L)}\right) \\ \mathbf{P}_{\text{tr}}^{(k,L)},\ otherwise \end{cases} \tag{13}$$

$$g_{\text{best}} = \min\left[E\left(\mathbf{P}_{\text{o}}^{(k,L)}\right), E\left(\mathbf{P}_{\text{new}}^{(k,L)}\right)\right],\ \forall\ k \tag{14}$$

where $E(\cdot)$ is the objective function as defined in Eq. (9), and g_{best} is the minimized objective value, directly reflecting the deviation between the margin of the micro-cracks and the envelope curve C_2. Moreover, the 1 by L vector $\mathbf{p}_{\text{best}}$ corresponding to the value g_{best} will be the best estimated unknown parameters in this step.

By replacing $\mathbf{P}_{\text{o}}^{(K,L)}$ with $\mathbf{P}_{\text{new}}^{(K,L)}$ and repeating the mutation, crossover, and selection phases, the minimization will iteratively run until the stop criteria is satisfied. After finishing the iteration, the final vector $\mathbf{p}_{\text{best}} = \left[\hat{\alpha}, \hat{\beta}, \hat{\gamma}, \hat{h}_{\text{c}}, \hat{x}_{\text{o}}, \hat{y}_{\text{o}}, \hat{\kappa}\right]$ will be the most proper parameters, and $\hat{h}_{\text{c}}$ is the identified critical DoC.

4. Numerical simulation

Numerical simulation is conducted to verify the feasibility of the proposed identification method. A curve governed by randomly chosen parameters $\mathbf{P}_1 = [0.5^{\circ}, 0.2^{\circ}, 0.09^{\circ}, 140\ nm, 10\ \mu m, 5\ \mu m, 2^{\circ}]$ is employed to mimic the envelope curve of the cracked region. For the DE minimization, the population size and iteration step are set as 30 and 100, respectively, and the crossover factor is 0.7. To investigate the practical working performance, uniformly randomized noise with a mean value of 6 μm and amplitude of 12 μm is superimposed on the envelope curve to simulate the extracted margin of the micro-cracks.

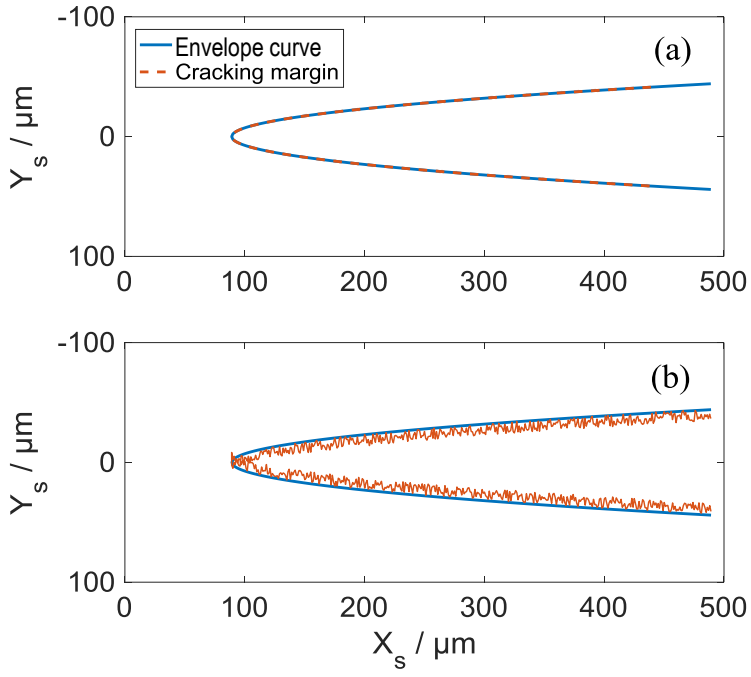

Figure 3: Simulation results, (a) without noises, and (b) with uniformly randomized noises.

Simulation for each case is conducted for 20 times, and the envelope curves and the margins of the micro-cracks after position transition are illustrated in Figs. 3 (a) and (b) with good fitness. As for the simulated margin without noise, a mean value of 139.90 nm with a standard deviation of 0.21 nm is achieved for the critical DoC. Compared with the pre-set true value(h_c = 140 nm), the deviation is only about 0.7 ‰. Similarly, as for the simulated margin with the noise, a mean

value of 139.51 nm with a standard deviation of 0.26 nm is achieved for the critical DoC, and the deviation of the mean value from the true one is about 3.5 ‰. It is slightly larger than the result obtained without noise but maintaining relative small. The numerical simulation result suggests that the proposed identification method has a very high identification accuracy with sub-nanometric uncertainty.

5. Experimental results and discussion

To experimentally investigate the feasibility of the proposed method, taper cutting of single crystal silicon is conducted on a ultra-precision machine tool (Moore nanotech 350FG, USA) by adopting a natural single crystal diamond tool (Contour Fine Tooling, UK). It has a nose radius of 1.549 mm and rake angle of -20°. The cutting speed is 0.5 mm/s. After cutting, features of the machined surface is captured through an optical microscope (BX60 Olympus, Japan).

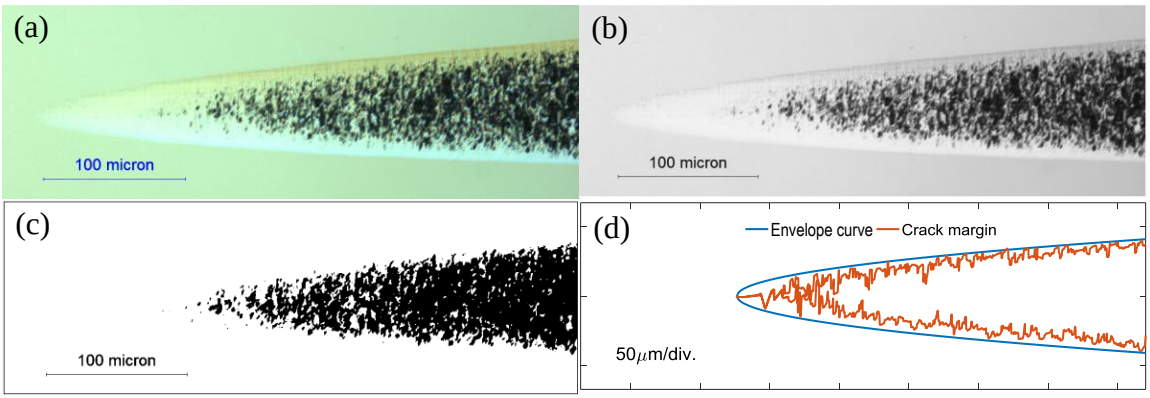

Figure 4: Features of the obtained surface, (a) the optical microscopic image, (b) the gray image, (c) the binary image, and (d) the identified envelop curve and the corresponding cracking margin.

First of all, the cutting velocity is oriented along the ⟨110⟩ direction. The obtained optical microscopic image is illustrated in Fig. 4 (a), and the corresponding gray and binary images are generated through image analysis as shown in Fig. 4 (b) and 4 (c), respectively. By using the binary image, features in the cracked region will be much more clear to facilitate extraction of the margin of the micro-cracks. The extracted margin and the identified envelope curve are given in

Fig. 4 (d), showing good agreement between each other. After conducting calculation for 20 times, the obtained mean value of the critical DoC is about 140.22 nm with a standard deviation of about 0.11 nm.

Moreover, taper cutting along the $\langle \bar{1}10 \rangle$ and $\langle 1\bar{1}0 \rangle$ directions is also conducted to further verify the universality of the proposed method. To avoid repetition, only the obtained gray images of the resulted surfaces in cutting along the two directions are illustrated in Fig. 5 (a) and 5 (c), and the extracted margins and the corresponding identified envelope curves are shown in Figs. 5 (b) and 5 (d), respectively. Similarly, the envelope curves fit well with the margins of the micro-cracks. The identified critical DoC for the two directions are 125.87 nm and 125.61 nm, and the corresponding standard deviations are about 0.42 nm and 0.52 nm. From the identified results, sub-nanometric uncertainties are obtained for all the three obtained surfaces, well demonstrating the effectiveness of the proposed method for identifying the critical DoC.

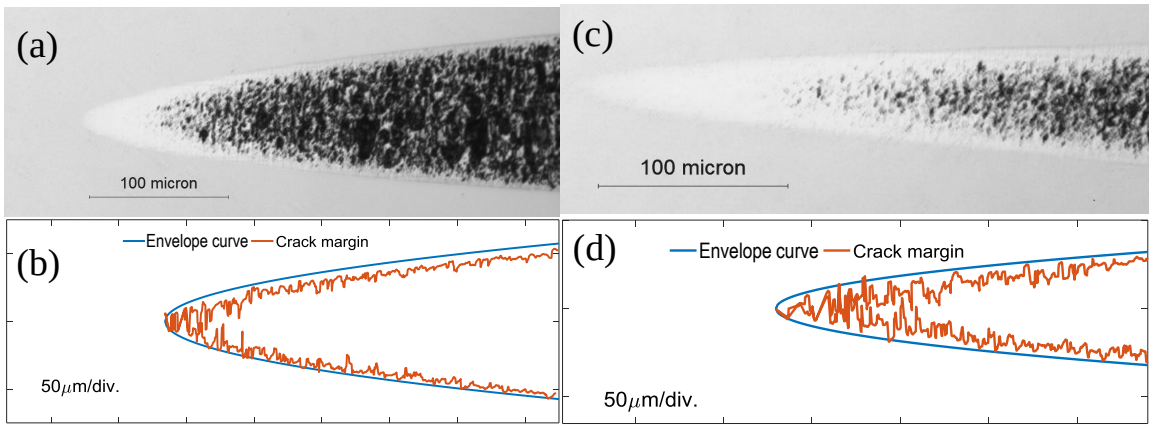

Figure 5: Characteristics of the obtained surfaces, (a) the gray image, and (b) the envelope curve and extracted margins of the surface obtained in cutting along the $\langle \bar{1}10 \rangle$ direction; (c) the gray image, and (d) the envelope curve and extracted margins of the surface obtained in cutting along the $\langle 1\bar{1}0 \rangle$ direction.

It is noteworthy that there are intermittent micro-cracks at the onset stage of the formation of the cracked region, which is especially evident for cutting using small inclination angles as illustrated in Fig. 4 and Fig. 5 (c). This chaotic region may contribute to the brittle-ductile transition as reported before [13]. From the identified envelope curves shown in Fig. 4 (d), Fig. 5 (b), and Fig. 5

(d), margins of the generated micro-cracks are well within the envelope curve for any positions in the cutting region, suggesting that even with the growth of lateral micro-cracks, the critical DoC that triggers the onset of the micro-cracks is almost unaffected. Moreover, there is also hybrid brittle-ductile region inner but close to the envelope curve, suggesting that the brittle-ductile transition region also occurs at CCPs when the practical DoC approaches to the critical DoC.

6. Conclusion

An identification method of the critical DoC is proposed based on the 2-D microscopic image of the cutting region resulted from taper cutting of brittle materials. It mainly consists of three stages: a) extraction of the margin of micro-cracks through image analysis; b) theoretical formulation of the projected curve of the cutting points on the imaging plane with respect to a specified DoC during the whole cutting process; c) minimization of the deviation between the theoretical curve and the margin of the micro-cracks through differential evolution algorithm.

To assess the proposed identification method, numerical simulation is firstly conducted by using an ideal profile as the crack margin, and the uniformly randomized noise is then superimposed on the profile to simulate the micro-cracks. For both cases, the obtained relative identification errors are less than 3.5 ‰ with uncertainty less than 0.3 nm. Practical cutting of single crystal silicon is then carried out along the $\langle 110 \rangle$, $\langle \bar{1}10 \rangle$, and $\langle 1\bar{1}0 \rangle$ directions. The identified critical DoCs are about 140.22 nm, 125.87 nm, and 125.61 nm, respectively. The corresponding uncertainties are about 0.11 nm, 0.42 nm, and 0.52 nm. Both numerical simulation and experimental results well demonstrate the effectiveness of the proposed identification method.

Acknowledgments

This work was jointly supported by the National Natural Science Foundation of China (51705254, 51675455), the Natural Science Foundation of Jiangsu Province (BK20170836), and the Fundamen-

tal Research Funds for the Central Universities (30917011301, 309171A8804).

References

[1] Z. Zhu, S. To, G. Xiao, K. F. Ehmann, G. Zhang, Rotary spatial vibration-assisted diamond cutting of brittle materials, Precision Engineering 44 (2016) 211–219.

[2] J. Owen, M. Davies, D. Schmidt, E. Urruti, On the ultra-precision diamond machining of chalcogenide glass, CIRP Annals-Manufacturing Technology 64 (1) (2015) 113–116.

[3] J. Yan, M. Yoshino, T. Kuriagawa, T. Shirakashi, K. Syoji, R. Komanduri, On the ductile machining of silicon for micro electro-mechanical systems (mems), opto-electronic and optical applications, Materials Science and Engineering: A 297 (1) (2001) 230–234.

[4] B. S. Dutterer, J. L. Lineberger, P. J. Smilie, D. S. Hildebrand, T. A. Harriman, M. A. Davies, T. J. Suleski, D. A. Lucca, Diamond milling of an alvarez lens in germanium, Precision Engineering 38 (2) (2014) 398 – 408.

[5] J. Yan, K. Maekawa, J. Tamaki, T. Kuriyagawa, Micro grooving on single-crystal germanium for infrared fresnel lenses, Journal of micromechanics and microengineering 15 (10) (2005) 1925.

[6] Z. Li, F. Fang, J. Chen, X. Zhang, Machining approach of freeform optics on infrared materials via ultra-precision turning, Optics Express 25 (3) (2017) 2051–2062.

[7] M. Mukaida, J. Yan, Ductile machining of single-crystal silicon for microlens arrays by ultra-precision diamond turning using a slow tool servo, International Journal of Machine Tools and Manufacture 115 (2017) 2 – 14.

[8] D. Yu, Y. Wong, G. Hong, Ultraprecision machining of micro-structured functional surfaces on brittle materials, Journal of micromechanics and microengineering 21 (9) (2011) 095011.

[9] Y.-L. Chen, Y. Cai, K. Tohyama, Y. Shimizu, S. Ito, W. Gao, Auto-tracking single point diamond cutting on non-planar brittle material substrates by a high-rigidity force controlled fast tool servo, Precision Engineering 49 (2017) 253–261.

[10] S. Goel, X. Luo, P. Comley, R. L. Reuben, A. Cox, Brittle–ductile transition during diamond turning of single crystal silicon carbide, International Journal of Machine Tools and Manufacture 65 (2013) 15–21.

[11] J. Yan, T. Asami, H. Harada, T. Kuriyagawa, Fundamental investigation of subsurface damage in single crystalline silicon caused by diamond machining, Precision Engineering 33 (4) (2009) 378–386.

[12] G. Xiao, S. To, G. Zhang, Molecular dynamics modelling of brittle–ductile cutting mode transition: Case study on silicon carbide, International Journal of Machine Tools and Manufacture 88 (2015) 214–222.

[13] M. Arif, Z. Xinquan, M. Rahman, S. Kumar, A predictive model of the critical undeformed chip thickness for ductile–brittle transition in nano-machining of brittle materials, International Journal of Machine Tools and Manufacture 64 (2013) 114–122.

[14] J. Wang, F. Fang, X. Zhang, An experimental study of cutting performance on monocrystalline germanium after ion implantation, Precision Engineering 39 (2015) 220–223.

[15] G. Xiao, S. To, E. Jelenković, Effects of non-amorphizing hydrogen ion implantation on anisotropy in micro cutting of silicon, Journal of Materials Processing Technology 225 (2015) 439–450.

[16] G. Xiao, Molecular dynamics modelling and mechanics analysis on the mechanism of brittle

to ductile cutting mode transition in ultra-precision machining, Ph.D. thesis, The Hong Kong Polytechnic University (2015).

[17] R. Storn, K. Price, Differential evolution–a simple and efficient heuristic for global optimization over continuous spaces, Journal of Global Optimization 11 (4) (1997) 341–359.

[18] A. K. Qin, V. L. Huang, P. N. Suganthan, Differential evolution algorithm with strategy adaptation for global numerical optimization, IEEE transactions on Evolutionary Computation 13 (2) (2009) 398–417.

List of Figures